

Modelling PAH curvature in laminar premixed flames using a detailed population balance model

Edward K. Y. Yapp¹, Clive G. Wells^{2,3}, Jethro Akroyd¹, Sebastian Mosbach¹, Rong Xu⁴, Markus Kraft^{1,4}

released: 24 May 2016

¹ Department of Chemical Engineering
and Biotechnology
University of Cambridge
New Museums Site
Pembroke Street
Cambridge, CB2 3RA
United Kingdom

² Centre for Mathematical Sciences
Wilberforce Road
Cambridge, CB3 0WA
United Kingdom

³ Hughes Hall
Cambridge, CB1 2EW
United Kingdom

⁴ School of Chemical and
Biomedical Engineering
Nanyang Technological University
62 Nanyang Drive
Singapore 637459

Preprint No. 161



Edited by

Computational Modelling Group
Department of Chemical Engineering and Biotechnology
University of Cambridge
New Museums Site
Pembroke Street
Cambridge CB2 3RA
United Kingdom

Fax: + 44 (0)1223 334796

E-Mail: c4e@cam.ac.uk

World Wide Web: <http://como.cheng.cam.ac.uk/>

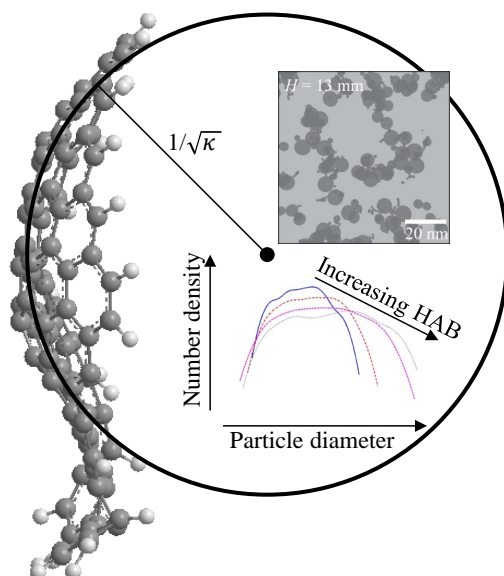


Highlights

- Modelling of the Gauss curvature of PAHs
- Given the number of 5- and 6-member rings in a PAH, the Gauss-Bonnet theorem can be used to estimate the average Gauss curvature (or radius of curvature) of the PAH, independent of where the 5-member ring is embedded within the PAH

Abstract

A detailed population balance model, which includes the kinetic Monte Carlo-aromatic site (KMC-ARS) model for detailed polycyclic aromatic hydrocarbon (PAH) growth, is used to compute the Gauss curvature of PAHs in laminar premixed ethylene and benzene flames. Previous studies have found that capping of an embedded 5-member ring causes curvature in graphene edges. In this work, a capping process is added to the KMC-ARS model with the rate coefficient of the capping reaction taken from the work of You *et al.* [Proc. Combust. Inst., 33:685–692, 2011]. We demonstrate that the Gauss-Bonnet theorem can be used to derive a correlation between the number of 5- and 6-member rings in a PAH and its Gauss curvature (or radius of curvature), independent of where the 5-member ring is embedded within the PAH structure. Numerical simulation yields satisfactory results when compared to the experimentally determined Gauss curvature reported in the literature. Computed and experimental fringe length distributions are also compared and the results suggest that PAHs smaller than the size required for inception are able to condense onto particles.



Contents

1	Introduction	3
2	Computational method	4
3	Detailed population balance model	5
4	Curvature	7
5	Results and discussion	9
6	Conclusions	15
A	Supplementary material	17
	References	21

1 Introduction

The buckminsterfullerene (C_{60}) was first discovered during the condensation of carbon vapour after the laser bombardment of graphite [29]; subsequently, C_{60} and other fullerenes were discovered in flames [25]. Fullerenes are a class of 3-D closed shells which contain exactly 12 pentagons. Their shape and size depends on the arrangement of pentagons as well as the number of hexagons. One can also consider them to be 2-D as the carbon atoms only form a molecular sheet [27]. Sheets containing less than 12 pentagons are open shells with the limiting case being a flat sheet. In a comment on the role of fullerenes in soot formation in flames, Frenklach and Ebert [19] argue that polycyclic aromatic hydrocarbons (PAHs) can curve through the incorporation of 5-member rings and can grow through sequential buildup of benzene and acenaphthylene to form fullerenes. They further argue that partially closed carbon clusters may collide and stick together while open shells continue to grow forming layers around the adducts; an explanation that is consistent with experimental high-resolution transmission electron microscopy (HRTEM) images of soot collected from flames which show multiple centres surrounded by concentric circles (see, *e.g.*, ref. [3, 8, 9, 26, 44]). Quantitative measurements of these sheet-like PAHs otherwise referred to as lattice fringes have been made including measurements such as the fringe length, interlayer spacing and, more rarely, radius of curvature [3, 26].

To model the 3-D evolution of PAH structures in different flame environments, Violi *et al.* [48, 50, 51] employ a fully-coupled kinetic Monte Carlo/molecular dynamics (KMC-MD) code which has a detailed PAH growth mechanism. Frenklach and co-workers [56, 57, 61] use a similar model which includes many more reactions creating 5- and 6-member complexes and more recently has been extended to include oxidation reactions [42]. However, these simulations are computationally very expensive. Therefore, these simulations are limited to the tracking of a single, non-interacting PAH; whereas experimental HRTEMs show that soot particles are made up of multiple layers of stacked PAHs. Kraft and co-workers employ a detailed population balance model [12] which is solved using a stochastic numerical method [5]. The model describes particles as aggregates composed of primary particles which are in turn composed of individual PAHs, thus containing information on particle size, morphology, and the internal structure of the particles. These particles undergo coagulation, sintering and particle rounding due to condensation and surface growth. This is the PAH-primary particle (PAH-PP) model [40]. The KMC-aromatic site (KMC-ARS) model tracks each of the PAHs in the particles which evolve according to a list of jump processes [33, 34] which make use of the steady-state assumption [21] for all intermediate species to reduce the computational expense of the simulations. This particular modelling approach has been used to simulate soot formation in laminar flames (see, *e.g.*, ref. [5, 12, 40, 59, 60]) and engines (see, *e.g.*, ref. [31]). The KMC-ARS model is unable to predict curvature because it does not allow the incorporation of 5-member rings and it only tracks the coordinates of the carbon atoms which describes the edge of the PAH. But the Gauss-Bonnet theorem [7, 24] which relates the integral of the Gauss curvature over a compact surface, *i.e.* its total Gauss curvature, with an integer naturally associated to it, *i.e.* its Euler characteristic, may be of help to us.

The purpose of this paper is to extend the PAH-PP/KMC-ARS model such that we can not only track PAHs but also allow the inclusion of 5-member rings and to track the as-

Table 1: Flame conditions

Flame	Unburned gas composition ^a				Equivalence ratio	Linear velocity ^b (cm/s)	Maximum flame temperature, T_m (K)	Burner temperature ^c (K)
	C ₂ H ₄	C ₆ H ₆	O ₂	N ₂				
A	0.444		0.556		2.4	4	1723	333
B		0.053	0.199	0.748	2.0	3	1713	333

^a Mole fractions.^b Under the STP conditions.^c Water-cooled burner.

sociated change in curvature using the Gauss-Bonnet theorem. Computed fringe length distributions are also compared with experimental measurements [3]. As fringe length is thought to be related to PAH size, these comparisons allows us to investigate the minimum PAH sizes required for inception and condensation which may be different. The influence of different fuels is also briefly studied. First, the flame chemistry and structure are computed using a steady-state burner-stabilised premixed laminar flame code. Second, the particle dynamics is solved using a detailed population balance model where the PAH growth mechanism is extended to allow for the incorporation of 5-member rings which leads to PAH curvature.

2 Computational method

The computational method consists of two parts. In the first part, species profiles are computed using a modified version of PREMIX [28], including calculation of the source terms by the method of moments with interpolative closure (MOMIC) using the code published by Revzan *et al.* [35]. The experimental temperature profile [15, 38] is imposed. The ABF mechanism, which includes combustion chemistry and the formation and growth pathways of PAHs up to pyrene, and species thermodynamics and transport properties [4, 53] are supplied as input. Note that the ABF mechanism includes the mechanism for benzene combustion. The transport equations of the moments of the particle size distribution (PSD) are solved to account approximately for the production and consumption of key gas-phase species due to inception, condensation, surface growth and oxidation. A total of six moments, including the zeroth moment, are solved using MOMIC to close the moment transport equations. In the second part, a detailed population balance model is applied as a post-processing step where the imposed temperature and computed species profiles from PREMIX are supplied as input.

We investigate two different flames and the flame conditions are summarised in Table 1. These are atmospheric pressure sooting flames where the main difference is that Flame A [15] is an ethylene flame ($\phi = 2.4$) while Flame B [38] is a benzene flame ($\phi = 2.0$). PREMIX simulations are performed using windward differencing and considering multicomponent transport and thermal diffusion. About 150 grid points are found to be sufficient for convergence.

3 Detailed population balance model

A detailed population balance model [12] is used to model soot formation by postprocessing the PREMIX simulations of the burner-stabilized laminar premixed flame. The growth of PAH species within the model is described by a kinetic Monte Carlo-aromatic site (KMC-ARS) model [33], starting from pyrene. The dynamics of the soot particle population are described by the Smoluchowski coagulation equation with additional terms for particle inception, condensation, sintering and surface growth. A brief description of the most important aspects of the particle model is given below. Further details may be found elsewhere [12, 33, 40, 60].

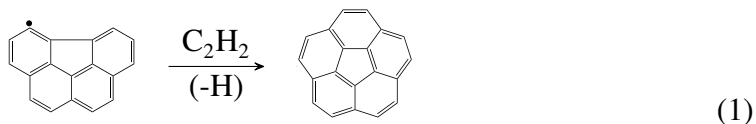
In the model, soot particles are represented as aggregates composed of primary particles, where each primary particle is composed of a number of PAHs. A primary particle is represented as a set of two or more PAHs. An aggregate is represented as a set of two or more primary particles. Each aggregate stores a list of neighbouring primary particles and resolves the common surface area between each pair of neighbours, where each pair of neighbours can be in point contact, can be fully sintered or can be anywhere in between [40]. This is the PAH-primary particle (PAH-PP) model [40]. The edge of each PAH is described by a list of contiguous site types [33]. These elementary sites include free-edge, zig-zag, armchair and bay sites [11, 18]. This representation allows the exact structure of each individual PAH to be resolved. This is the KMC-ARS model [33] and both models are solved by the kinetic Monte Carlo method. First the rates of inception, coagulation and condensation are calculated, and a particle pair is selected stochastically. The KMC-ARS model which is composed of 21 jump processes [60]—where intermediate species are assumed to be in steady state [21]—that describes the growth of PAHs, iterates through each PAH in the selected particle pair, calculates the total rate of these jump processes, and again selects a jump process stochastically. Note that the growth of PAHs in the gas phase and in particles are fully coupled [12]. Finally, once all the PAHs in each particle are updated, sintering and subsequently the chosen particle process are performed.

There are many parameters in the model, but the key parameters we investigate in this work are given in Table 2. Ranges within which these parameters are expected to vary and the initial values chosen for the base case simulations are shown. These are the same parameter values as in ref. [60] with the exception of the critical number of PAHs in a primary particle before the growth factor is applied, n_{crit} . The growth factor, g , is intended to account for the possibility that PAHs in large primary particles grow more slowly than PAHs in the gas phase. Totton *et al.* [45] showed that the average stack size for clusters of coronene molecules is around 4. Since reactions take place on the edge of a molecule and the edges of PAHs in stacks are exposed to the chemical environment, we assume that PAHs in stacks of up to 4 PAHs grow at the same rate as PAHs in the gas phase.

Whitesides and Frenklach [56] presented a detailed KMC-MD model of graphene-edge growth with a total of 42 surface transformations. One of the most interesting among them is capping which is the addition of acetylene to an embedded 5-member ring which causes a PAH to curve [23]:

Table 2: Model parameters in detailed population balance model.

Parameter	Range	Value
1) Minimum number of 6-member aromatic rings in a PAH for inception	-	16
2) Minimum number of 6-member aromatic rings in a PAH for condensation	-	16
3) Minimum number of 6-member aromatic rings in a PAH in a particle ($n_{\text{PAHs}} \geq n_{\text{crit}}$) below which it is removed	-	16
4) Soot density, ρ	$1 \text{ g cm}^{-3} \leq \rho \leq 2 \text{ g cm}^{-3}$	1.88 g cm^{-3}
5) Smoothing factor, σ	$0 \leq \sigma \leq 2$	1.69
6) Growth factor, g	$0 \leq g \leq 1$	0.0263
7) Critical number of PAHs in a primary particle before the growth factor is applied, n_{crit}	≥ 2	4
8) Sintering model:		
- A_s	-	$1.1 \times 10^{-14} \text{ s m}^{-1}$
- E_s	$1.8 \times 10^4 \text{ K} \leq E_s \leq 1.8 \times 10^5 \text{ K}$	$9.61 \times 10^4 \text{ K}$
- $d_{\text{pri,crit}}$	$1 \text{ nm} \leq d_{\text{pri,crit}} \leq 5 \text{ nm}$	1.58 nm



In this paper, hydrogen abstraction and the subsequent capping are represented as a jump process and is added to the KMC-ARS model. A complete list of jump processes, their steady-state rate expressions and the corresponding elementary reaction rate coefficients in the KMC-ARS model are given in the [Supplementary material](#) (Tables S1 and S2). The rate coefficient of reaction 1 is taken from the work of You *et al.* [61] who derived the coefficient using quantum-chemical calculations and reaction rate analysis. The coefficient has an order-of-magnitude accuracy. This coefficient is essential to predicting the capping of an embedded 5-member ring. We find that a rate coefficient estimated based on an analogous acetylene addition and cyclisation on a zig-zag site [23, 58] is about two orders of magnitude lower resulting in embedded 5-member rings migrating to adjacent zig-zag sites (jump process S17) and subsequently desorbing (jump process S6) instead of being capped.

By describing the edge of each PAH through a list of site types alone, curved PAHs can be accommodated within the KMC-ARS model. However, updating the structure of the PAH depends on whether any “bridges” are present. The simplest example of a bridge is the C–C bond that joins two benzene rings in a biphenyl molecule. At this stage, we are unable to determine on-the-fly the location of any bridges from a list of site types

alone. Therefore, we exclude jump processes which create bridges, *i.e.*, phenyl addition and armchair oxidation by O₂ and OH. Before the inclusion of reaction 1, phenyl addition constitutes less than 4 % of the total number of jump processes.

4 Curvature

As the KMC-ARS model gives us the number of capped 5-member rings we need to develop a theory which allows us to calculate the curvature of the PAH surface if we want to compare the molecular structure of the soot particles with measured data. The Gauss-Bonnet theorem relates the curvature of a surface to its Euler characteristic, which is a number that describes the structure of a PAH in terms of vertices, edges and faces. Given the number of 5- and 6-member rings in a PAH, we demonstrate how this theorem can be used to estimate the average Gauss curvature (or radius of curvature) of the PAH, independent of where the 5-member ring is embedded within the PAH.

Consider a PAH molecule comprising P pentagons and H hexagons. Associate with each interior atom a curvature κ_{PPP} , κ_{PPH} , κ_{PHH} or κ_{HHH} depending on whether the atom is part of three pentagons, two pentagons and a hexagon, one pentagon and two hexagons, or three hexagons. The probabilities that an interior point selected at random will be each of these types are:

$$\mathbb{P}_{PPP} = F(3); \quad \mathbb{P}_{PPH} = F(2); \quad \mathbb{P}_{PHH} = F(1); \quad \mathbb{P}_{HHH} = F(0); \quad (2)$$

where F is the hypergeometric distribution

$$F(p) = \frac{\binom{P}{p} \binom{H}{3-p}}{\binom{P+H}{3}}, \quad (3)$$

parameterised by p which is the number of pentagons an interior atom is part of. As a rule of thumb the hypergeometric distribution should be considered when the sample size ($= 3$) is larger than approximately 10 % of the population [10], or 30 aromatic rings or less. Now assign the average Gauss curvature of the PAH molecule to be

$$\bar{K} = \kappa_{PPP}\mathbb{P}_{PPP} + \kappa_{PPH}\mathbb{P}_{PPH} + \kappa_{PHH}\mathbb{P}_{PHH} + \kappa_{HHH}\mathbb{P}_{HHH}. \quad (4)$$

When $P = 0$ the molecule is flat and hence $\kappa_{HHH} = 0$. The Gauss curvature is defined to be

$$K = \kappa_1 \kappa_2 = (R_1 R_2)^{-1}, \quad (5)$$

where κ_1 and κ_2 are the principal curvatures, and R_1 and R_2 are the principal radii of curvature. Figure 1 illustrates the concept of principal curvatures and radii of curvatures at a given point along a surface. X_1 and X_2 are unit vectors tangent to the surface pointing in the direction along which the maximum and minimum curvatures κ_1 and κ_2 are found, hence, the name principal curvatures. The inverse of these curvatures are the principal radii of curvature and can be understood as the radius of a circle that best approximates the

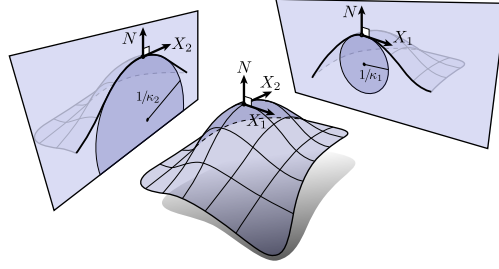


Figure 1: *The Gauss curvature is defined as the product of the two principal curvatures κ_1 and κ_2 at any given point along a surface. X_1 and X_2 are unit vectors tangent to the surface along which the maximum and minimum curvatures are found and N is the unit vector normal to the surface. Used with permission [16].*

curve at that point. N is the unit vector normal to the surface. We will require that Eq. (4) holds for three arrangements of pentagons and hexagons that allow us easy computation of the average Gauss curvature. The Gauss-Bonnet theorem for a closed surface is:

$$2\pi\chi = \int_M K dS = \bar{K} \int_M dS = \bar{K}S, \quad (6)$$

where χ is the Euler characteristic, M is any two-dimensional Riemannian manifold, dS is the area element of the surface and S is the total surface area. We will apply this when M is a closed surface and $\chi = 2$ (for a topological sphere). In particular we will consider the dodecahedrane, the buckminsterfullerene and the rugbyballene which consist of 20, 60 and 70 carbon atoms respectively as shown in Fig. 2. Let our hexagons and pentagons

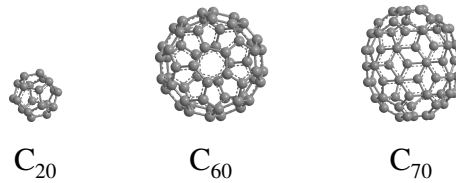


Figure 2: *Various closed surfaces which display a range of curvatures.*

have side length a ($= 1.395 \text{ \AA}$, the length of an aromatic C–C bond [21]), then the areas of the pentagon and hexagon are

$$A_P = \frac{1}{4} (5(5 + 2 \times 5^{1/2}))^{1/2} a^2 \quad \text{and} \quad A_H = \frac{3 \times 3^{1/2}}{2} a^2. \quad (7)$$

For the dodecahedrane $P = 12$ and $H = 0$, so that $\bar{K} = \kappa_{PPP}$ and from the Gauss-Bonnet theorem we have

$$\kappa_{PPP} = \pi / (3A_P). \quad (8)$$

Combining the results for the buckminsterfullerene ($P = 12$ and $H = 20$) and rugbybal-

lene ($P = 12, H = 25$) we get

$$\kappa_{PPH} = \frac{992\pi}{55(3A_P + 5A_H)} - \frac{19684\pi}{275(12A_P + 25A_H)} - \frac{22\pi}{225A_P}, \quad (9)$$

$$\kappa_{PHH} = \frac{11\pi}{450A_P} - \frac{124\pi}{15(3A_P + 5A_H)} + \frac{1036\pi}{25(12A_P + 25A_H)}. \quad (10)$$

In summary, given the number of 5- and 6-member rings in a PAH, Eqs. (2–4, 7–10) can be used to estimate the average Gauss curvature of each PAH. Assuming that points on the surface are locally spherical (umbilical points), the principal radii of curvature are equal ($K = \bar{K}$) and Eq. (5) can be used to estimate the radius of curvature as $R_c = \bar{K}^{-1/2}$.

5 Results and discussion

The computed structure of flame A is shown in the left column of Fig. 3. It is qualitatively similar to other laminar premixed ethylene flames modelled using a similar gas-phase chemical mechanism [55]. Soot volume fraction measurements show that soot first appears at a height above the burner, H , of around 0.2 cm [15]. This is consistent with the location where fuel and oxidiser are predicted to disappear and where there is a sharp increase in the PAH concentrations. We see a rise-then-fall in the profile of pyrene because of its consumption from particle inception and condensation on soot surfaces. Also shown in Fig. 3 (right column) is the computed structure of flame B. There are two differences which are important for reasons which will be discussed later. First, the maximum temperature, T_m , is 10 K lower than that measured for flame A at 1713 K. Second, the concentration of the C_2H_2 growth species is about an order-of-magnitude lower which is expected because the benzene fuel has to be oxidised to form C_2H_2 whereas only one hydrogen molecule has to be removed from ethylene [6]. Therefore, we would expect surface growth to be slower in flame B than in flame A. However, we expect soot to be formed more easily in flame B, despite the lower equivalence ratio, because formation of the first aromatic ring is considered to be the first step towards the formation of soot [20].

HRTEM images were collected at several heights above the burner of both flames A and B [3]. Fringe analysis was performed on these images and the radius of curvature was then extracted from the fringes [3]. A limitation of radius of curvature, R_c , is that it is unbounded: R_c is infinite for a planar PAH; whereas Gauss curvature, K , is bounded between 0 for a planar PAH and around 31 nm^{-2} for a dodecahedrane, the smallest possible fullerene. For this reason, a comparison between experimental and computed average Gauss curvature for flames A and B is made in Fig. 4. (Equation (5) is used to convert the experimental radius of curvature to Gauss curvature.) The Gauss curvature of a dodecahedrane and the well-known buckminsterfullerene ($K \sim 9 \text{ nm}^{-2}$) are also shown. Experimentally, the average radius of curvature necessarily excludes “nearly” straight PAHs which would skew the average towards the straight PAHs. Therefore, the Gauss curvature is calculated as an average across PAHs in particles where at least one 5-member ring has been embedded and subsequently capped. Numerical simulation yields satisfactory results when compared to the experimentally determined Gauss curvature, in fact, the average Gauss curvature between the two flames are similar as will be discussed later.

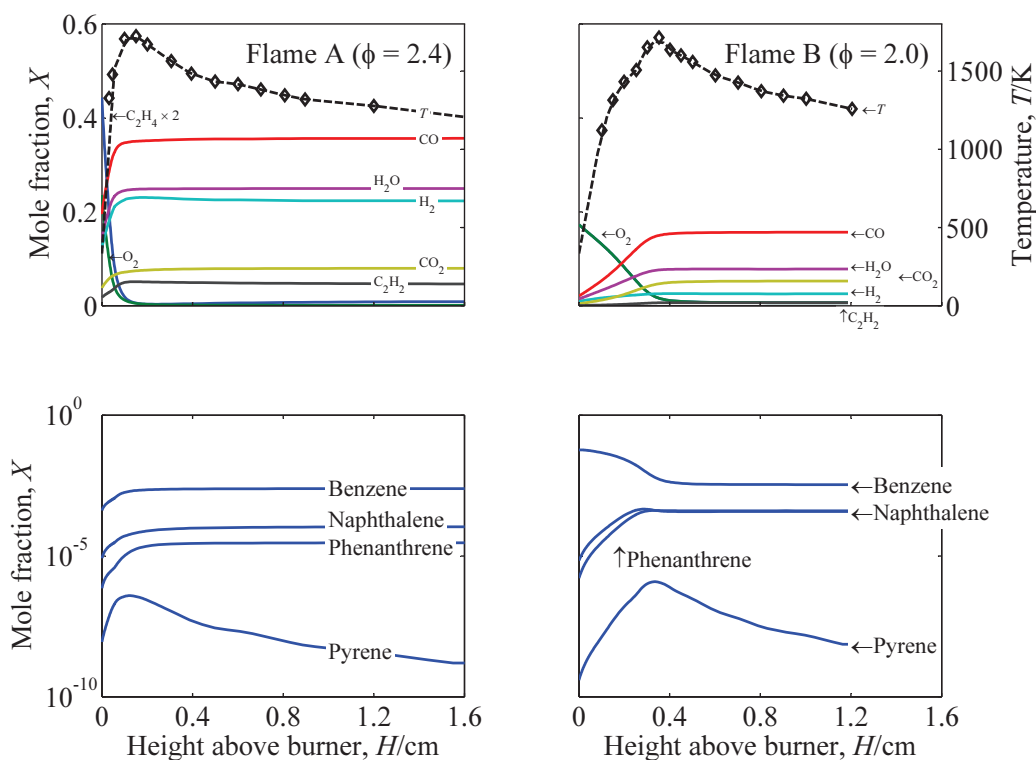


Figure 3: Computed mole fraction profiles of the major gas-phase species and selected aromatic species for flame A (left column) and flame B (right column) and the temperature measured by a silica-coated fine wire 25 μm Pt/Pt-13%Rh thermocouple (flame A [15] and flame B [38]).

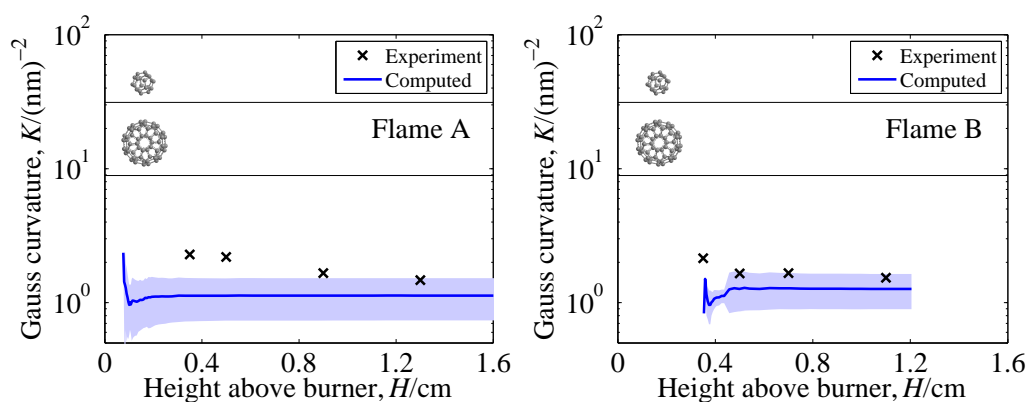


Figure 4: Comparison of the experimental (symbols) and computed (line) average Gauss curvature of PAHs in particles for flame A (left panel) and flame B (right panel). The shaded areas represent \pm one standard deviation in the computed distribution. The horizontal lines represent the Gauss curvature of a dodecahedrane ($K \sim 31 \text{ nm}^{-2}$) and buckminsterfullerene ($K \sim 9 \text{ nm}^{-2}$).

For these simulations we assume that only PAHs with 16 or more aromatic rings are able to stick because, in previous work [60], it provided the best fit against optical band gap

derived from extinction measurements [1]. (Optical band gap can be correlated with the number of aromatic rings in PAHs [37].) We find that assuming pyrene dimerisation as the inception step results in no curved PAHs because PAHs do not have sufficient time to grow and incorporate 5-member rings before they form a particle where growth is essentially frozen (growth factor, $g = 0.0263$). Note that the approach used in this work to compute Gauss curvature is valid even for the very flat molecules that are observed because as long as the number of pentagons and hexagons is approximately less than 30, a very flat molecule would have a correspondingly small Gauss curvature.

To better understand the computed Gauss curvature results, the underlying raw data should be informative. Figure 5 shows the distribution of the number of embedded 5-member rings which are capped in PAHs in soot for flame A at $H = 13$ mm (top panel) and for flame B at $H = 11$ mm (bottom panel). Note that the length of the bars in each pattern represents the number of embedded 5-member rings which are capped as opposed to the number of PAHs. Both distributions show that there is a large concentration around PAHs which contain 16 6-member aromatic rings—a direct result of the inception/condensation threshold chosen (see parameters 1 and 2 in Table 2)—which explains why the average Gauss curvature in Fig. 3 for flames A and B are similar. Due to the higher temperature and concentration of the C_2H_2 growth species in flame A as compared to flame B, PAHs in flame A tend to be larger and incorporate up to three 5-member rings.

As an independent means of assessing the model’s ability to predict curvature, we optimise the structures of two representative PAHs predicted by the model in a post-analysis step and make a qualitative comparison with their respective Gauss curvatures. Geometry optimisation is performed using the MM2 [2] minimisation tool in Chem3D 15.1 [43]. While the MM3 potential is known to predict equilibrium bond lengths for fullerenes significantly better than MM2 [32], the optimisation is only performed for illustrative purposes therefore MM2 is deemed to be sufficient for these purposes. By tracking the evolution of the list of site types which describes the edge of each PAH as it undergoes surface growth, we are able to determine the exact structure of both PAHs. Figure 6 shows the most curved structure for flames A and B and the corresponding Gauss curvatures are 3.41 nm^{-2} (16 hexagons and 3 pentagons) and 2.36 nm^{-2} (16 hexagons and 2 pentagons). The structure from flame A has a higher Gauss curvature and its optimised structure does indeed look more curved than the structure from flame B, which provides some reassurance of the validity of the model.

A final note should be made about the Gauss curvature correlation derived in Section 4. The correlation is based upon the interpolation of the curvatures of different fullerenes. (At any point along the surface of a fullerene it has a non-negative curvature.) Therefore, implicit in the application of the correlation is the assumption that the PAH structure is either flat or bends in the same direction. Evidence of negative curvature (a saddle point or imagine a pringle-like surface) has occasionally been observed, for example, at the transition between conical and tubular sections of soot collected from a laminar benzene premixed flame [26] and is attributed to the presence of 7-member aromatic rings [30]. However, the structures identified within soot particles using HRTEM are either nearly straight or exhibit a positive overall curvature [3]. Application of the Gauss curvature correlation to the PAH structures predicted by the KMC-ARS model is also consistent because the KMC-ARS model only allows for the formation of 5- and 6-member aromatic

rings.

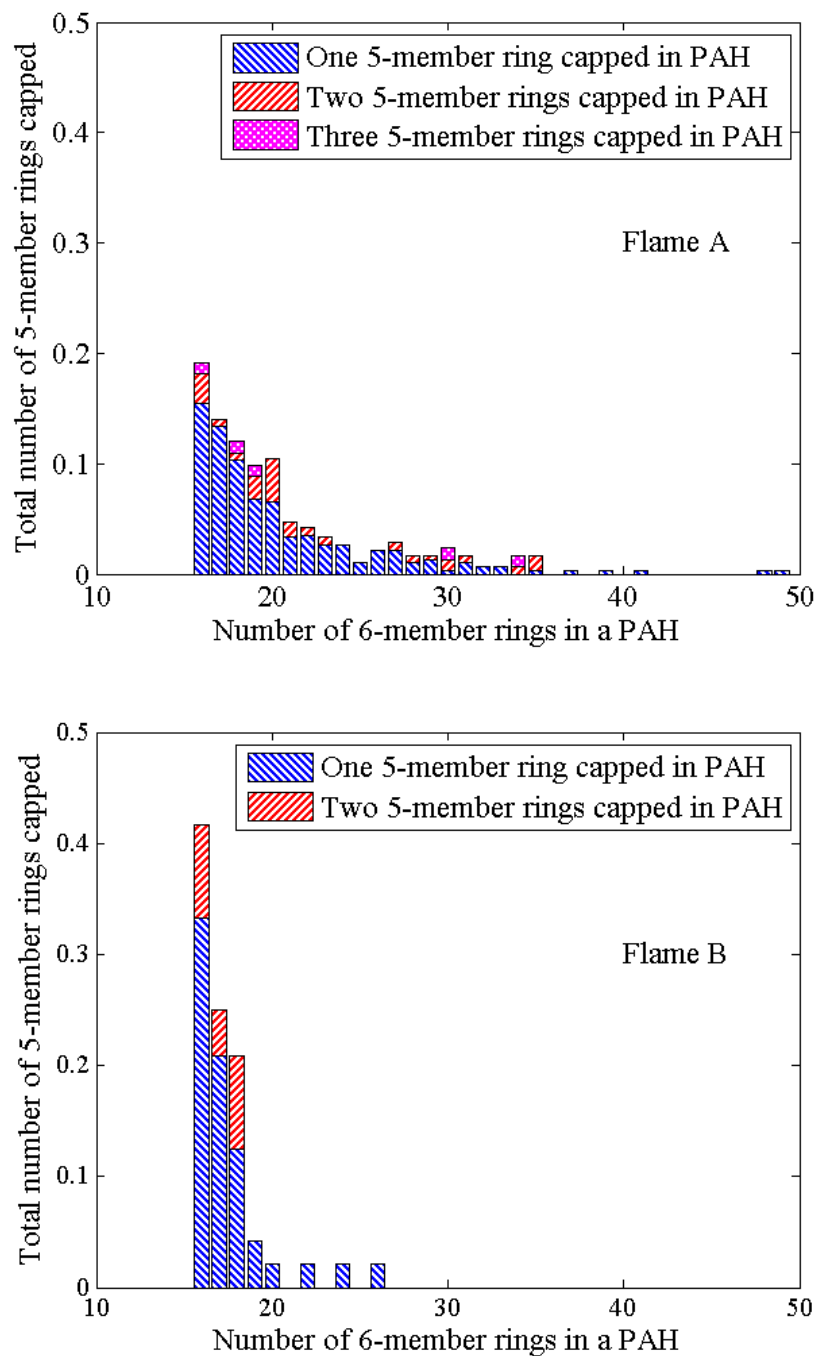


Figure 5: The number of embedded 5-member rings capped within PAHs in particles, sorted by the number of 6-member rings in the PAH, for flame A at $H = 13$ mm (top panel) and for flame B at $H = 11$ mm (bottom panel). The length of the bars in each pattern represents the number of embedded 5-member rings which are capped. (For interpretation of the references to colour in this figure legend, the reader is referred to the web version of this article.)

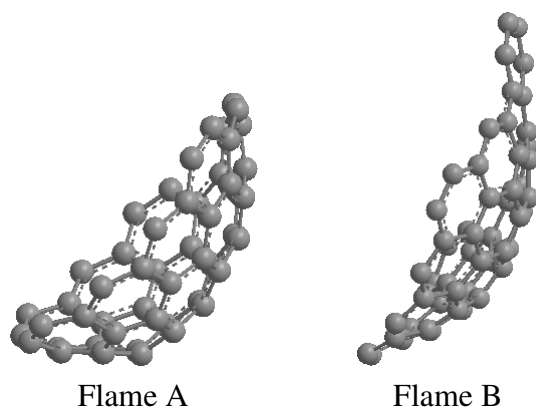


Figure 6: Representative structures predicted by the model and optimised using Chem3D 15.1 [43].

Fringe length distributions are useful as they have been used to provide insight to the molecules that are available for particle nucleation and surface growth [44]. Figure 7 (left column) shows experimental fringe length distributions at two heights above burner representing nascent and mature soot for flames A and B. It was initially surprising that the

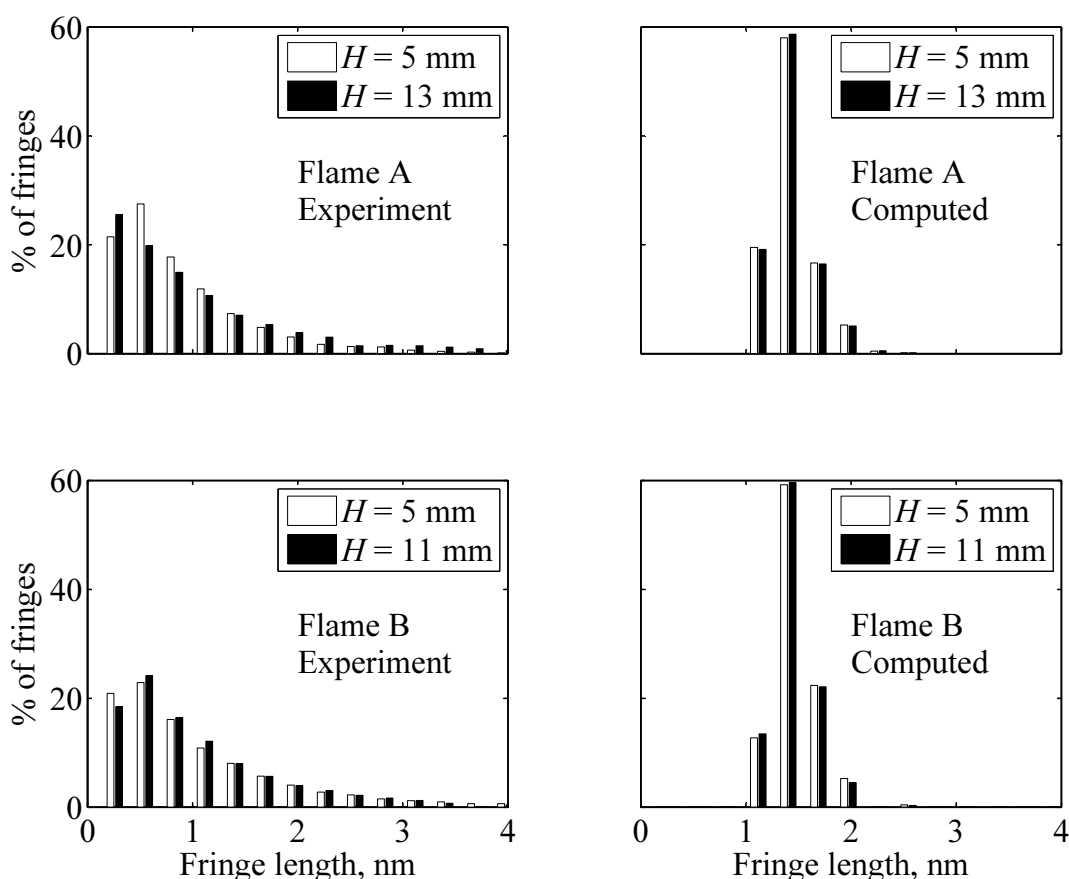


Figure 7: Comparison of experimental [3] (left column) and computed (right column) fringe length distributions at two heights above the burner representing nascent (unfilled) and mature (filled) soot for flames A (top row) and B (bottom row).

distributions are relatively independent of fuel and maturity of the soot particles; however, similar results were found by Botero et al. [9], albeit for a laminar diffusion flame, where the average fringe length measured across a range of fuels and positions in the flame were practically indistinguishable.

Also shown in Fig. 7 (right column) are the computed fringe length distributions for planar PAHs, that is, before the inclusion of reaction 1. This approximation is made because it is not clear how a representative length can be easily extracted from a curved PAH; however, the majority of the computed PAHs are either flat or, as shown in Fig. 4, just slightly curved. We estimate the fringe length of each PAH structure as the arithmetic mean of its length and width [3]. There is a qualitative agreement between model and experiment where larger fringes are present in increasingly smaller quantities, but—more importantly—the distributions appear to be relatively independent of fuel or height which is observed experimentally. Quantitatively, however, the distributions differ notably. The smallest predicted fringe length is about 1.1 nm which corresponds to a PAH with 16 aromatic rings; it is assumed that only PAHs with 16 or more aromatic rings are able to incept or condense. Experimentally, all fringes larger than the size of one aromatic ring are considered [3]; therefore, the experimental distributions begin at about 0.3 nm. One of the steps in fringe analysis is establishing a minimum fringe length to rule out artifacts [47]. This is usually set at the size of benzene [3] or pyrene [47].

Are fringes the size of pyrene, or even benzene, physically reasonable? There have been a number of studies investigating theoretical aspects of PAH dimerisation as the initial step to particle nucleation. Sabbah et al. [39] found that the equilibrium of pyrene dimerisation strongly favours the dissociation of the dimer at high temperature and that much larger PAHs, PAHs the size of circumcoronene, are required to be able to play a role in nucleation [13, 14, 46, 52]. A key assumption made, however, is that dimerisation is governed by equilibrium kinetics. The next question that follows is are PAHs smaller than the size required for inception able to condense onto a particle? Laser microprobe mass spectrometry of nascent soot particles collected from a laminar ethene diffusion flame shows that masses the size of pyrene are present in significant quantities [17]. Schuetz and Frenklach [41] studied the non-equilibrium dynamics of binary collisions between pyrene molecules and found that development of internal rotors are sufficient to stabilise a pyrene dimer long enough to grow in size due to chemical reactions. While it is argued [52] that it is unclear whether a dimer is able to survive collision with gas phase molecules as most of these collisions are non-reactive, this hypothesis is plausible for the condensation of a pyrene molecule onto a larger, more stable PAH cluster [13, 14]. In order to reconcile experimental and computed soot volume fraction in a opposed-jet ethylene diffusion flame, Wang et al. [54] argued that aromatic species such as benzene and naphthalene may condense readily onto the soot surface. We test the hypothesis that PAHs smaller than the PAH size required for inception (16 rings) are able to condense onto a particle. Figure 8 shows the computed fringe length distribution for flame A at $H = 13$ mm for the base case and when the condensation threshold is lowered to 4 rings which goes some way towards reconciling the discrepancy with the experiments. The results for flame B are similar and a condensation threshold of 4 rings is chosen because pyrene is the gas-phase transfer species. The results suggest that species as small as pyrene could condense successfully onto a particle.

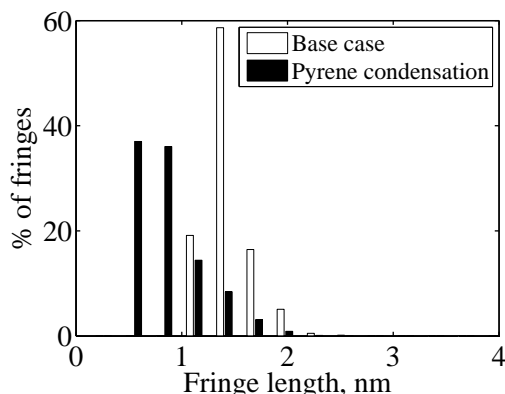


Figure 8: Sensitivity of the computed fringe length distributions to the condensation threshold for flame A at $H = 13$ mm.

6 Conclusions

A detailed population balance model, which includes the kinetic Monte Carlo-aromatic site (KMC-ARS) model for detailed polycyclic aromatic hydrocarbon (PAH) growth, is used to compute the Gauss curvature of PAHs in laminar premixed ethylene and benzene flames. We demonstrate that the Gauss-Bonnet theorem can be used to predict the Gauss curvature of PAHs in soot. The theorem is used to derive a correlation between the number of 5- and 6-member rings in a PAH and its Gauss curvature, independent of where the 5-member ring is embedded within the PAH structure. As a proof of concept, a single-step transformation which caps embedded 5-member rings in a PAH is added to the KMC-ARS model with the rate coefficient of the capping reaction taken from literature. Alternative pathways will be added in future. To accommodate the modelling of curved PAHs, we describe the edge of each PAH through a list of site types alone. There is a satisfactory agreement between the simulated and experimentally determined Gauss curvature reported in the literature. While the average Gauss curvature between the ethylene and benzene flames are similar, the model predicts that larger curved PAHs which incorporate more 5-member rings are formed in the ethylene flame. This may be explained by the higher temperature and computed concentration of the C_2H_2 growth species in the ethylene flame as compared with the benzene flame. Since the model resolves the structure of each PAH, we can extract a characteristic length from each PAH which can be compared with experimental fringe length distributions. It is found that assuming that only PAHs with 16 or more aromatic rings are able to dimerise or condense onto a particle leads to an overestimation of the smallest fringe length. Lowering the condensation threshold to pyrene improves the agreement with the experimental measurements. The results suggest that PAHs smaller than the size required for inception are able to condense onto particles.

Acknowledgement

The authors are grateful to three anonymous reviewers and to Professor Christof Schulz for offering his insight. Financial support by the Gates Cambridge is gratefully acknowl-

edged. This research is supported by the National Research Foundation, Prime Minister's Office, Singapore under its CREATE programme. Professor Markus Kraft has been supported by the Weierstrass Institute for Applied Analysis and Stochastics.

A Supplementary material

Table S1: Elementary reaction rate coefficients at atmospheric pressure

No.	Reactions ^b	$k = AT^n \exp(-E/RT)^a$			References
		A	n	E	
<i>Hydrogen abstraction from, and addition to, free-edges, zig-zags, armchairs and bays</i>					
1	$C_s-H+H \rightleftharpoons C_s^\bullet + H_2$	4.20×10^{13}		13.0	[4]
-1a	$C_s^\bullet + H_2 \rightarrow C_s + H$	3.90×10^{12}		11.0	[35]
-1b	$C_s^\bullet + H_2 \rightarrow C_s + H$	5.53×10^{12}		11.83	[56]
2	$C_s+H \rightleftharpoons C_s^\bullet + H_2$	9.24×10^7	1.50	9.646	[33]
-2	$C_s^\bullet + H_2 \rightarrow C_s + H$	9.60×10^4	1.96	9.021	[33]
3	$C_s-H+H \rightleftharpoons C_s^\bullet + H_2$	7.25×10^7	1.76	9.69	[49]
4	$C_s-H+H \rightleftharpoons C_s^\bullet + H_2$	1.74×10^8	1.74	9.37	[49]
5	$C_s-H+H \rightleftharpoons C_s^\bullet + H_2$	7.81×10^7	1.772	10.33	[34]
6	$C_s^\bullet + H \rightarrow C_s$	2.00×10^{13}		0	[4]
7	$C_sR6H^\bullet \rightarrow C_sR6 + H$	1.23×10^{10}	1.41	85.2	[49]
8	$C_s-H+OH \rightleftharpoons C_s^\bullet + H_2O$	1.00×10^{10}	0.734	1.43	[4]
-8	$C_s^\bullet + H_2O \rightarrow C_s-H+OH$	3.68×10^8	1.139	17.1	[35]
<i>Hydrogen abstraction from, and addition to, 5-member rings</i>					
9	$C_sR5+H \rightleftharpoons C_sR5^\bullet + H_2$	5.06×10^7	1.93	12.96	[23]
-9	$C_sR5^\bullet + H_2 \rightarrow C_sR5 + H$	1.28×10^6	1.93	62.34	c
10	$C_sR5^\bullet + H \rightarrow C_sR5$	6.08×10^{12}	0.27	0.280	[23]
11	$C_sR5+H \rightleftharpoons C_sR5H^\bullet$	8.41×10^8	1.490	0.992	[23]
-11	$C_sR5H^\bullet \rightarrow C_sR5 + H$	3.81×10^{11}	0.49	59.05	c
<i>S1: Free-edge ring growth</i>					
12	$C_s^\bullet + C_2H_2 \rightarrow C_sC_2H_2^\bullet$	1.10×10^7	1.61	3.896	[11]
<i>S2: Armchair ring growth</i>					
13	$C_s^\bullet + C_2H_2 \rightarrow C_s-H+H$	8.00×10^7	1.56	3.8	[4]
<i>S3: Free-edge ring desorption</i>					
14	$C_sR6^\bullet + 2H \rightarrow C_s^\bullet + 2C_2H_2$	1.30×10^{11}	1.08	70.40	[23]
<i>S4: 6- to 5-member ring conversion at armchair</i>					
15	$C_sR6^\bullet + H \rightarrow C_sR5 + C_2H_2$	1.30×10^{11}	1.08	70.40	$k_{16} = k_{15}$
<i>S5: 5-member ring addition to zig-zag</i>					
16	$C_s^\bullet + C_2H_2 \rightarrow C_sR5 + H$	6.80×10^{11}		22.02	[22]
<i>S6: 5-member ring desorption</i>					
17	$C_sR5^\bullet \rightarrow C_sC_2H_2^\bullet$	1.60×10^{14}		42.42	[22]
<i>S8: 5- to 6-member ring conversion at armchair</i>					
18	$C_sR5H^\bullet \rightarrow C_sR6 + H$	1.34×10^{12}		0	k_∞ (2000 K), [23]
<i>S9 and S10: Free-edge oxidation</i>					
19	$C_sR6^\bullet + O_2 \rightarrow C_sC_2H + HCO + CO$	2.10×10^{12}		7.47	[53]
20	$C_sR6 + OH \rightarrow C_sC_2H + CH_2CO + H$	1.30×10^{13}		10.6	[53]
<i>S11 and S12: Armchair oxidation</i>					
21	$C_sR6^\bullet + O_2 \rightarrow C_s^\bullet + 2CO$	2.10×10^{12}		7.47	$k_{22} = k_{20}$
22	$C_sR6 + OH \rightarrow C_s^\bullet + CH_2CO$	1.30×10^{13}		10.6	$k_{23} = k_{21}$
<i>S13: Benzene addition</i>					
23	$C_s^\bullet + C_6H_6 \rightleftharpoons C_sC_6H_5 + H$	2.22×10^{83}	-20.79	46.89	[36]
<i>S14: 5-member ring migration</i>					
24	$C_sR5H^\bullet \rightarrow C_sR5 + H$	1.34×10^{12}		0	$k_{25} = k_{19}$
<i>S15: 6-member bay closure</i>					
25	$C_s^\bullet \rightarrow C_sR6^\bullet$	1.11×10^{11}	0.658	23.99	[33]
<i>S16: 5-member bay closure</i>					
26	$C_s^\bullet \rightarrow C_sR5H$	3.86×10^{11}	0.21	17.7	[49]

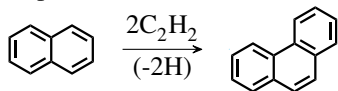
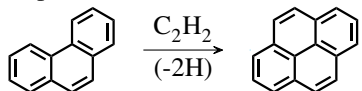
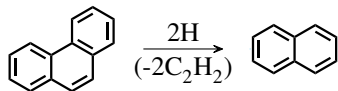
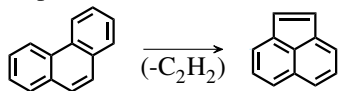
No.	Reactions ^b	$k = AT^n \exp(-E/RT)^a$			References
		A	n	E	
	<i>S17: Embedded 5-member ring migration</i>				
27	$C_5R5R6^\bullet \rightarrow C_5R6R5^\bullet$	4.96×10^{11}	0.755	50	[49]
	<i>S18: 6-member ring desorption at bay</i>				
28	$C_5R6^\bullet \rightarrow C_5(C_2H)C_2H_2^\bullet$	2.30×10^9	1.603	61.85	[34]
	<i>S20 and S21: Zig-zag oxidation</i>				
29	$C_5R6^\bullet + O_2 \rightarrow C_5^\bullet + \text{products}$	2.10×10^{12}		7.47	$k_{30} = k_{20}$
30	$C_5R6 + OH \rightarrow C_5^\bullet + \text{products}$	1.30×10^{13}		10.6	$k_{31} = k_{21}$
	<i>S22: Capping of embedded 5-member ring</i>				
31	$C_5^\bullet + C_2H_2 \rightarrow C_5R6 + H$	1.00×10^{10}	0.955	10.6	[61]

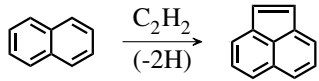
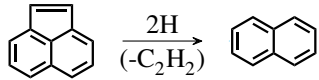
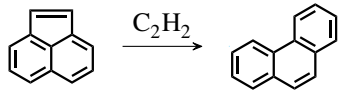
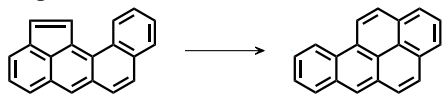
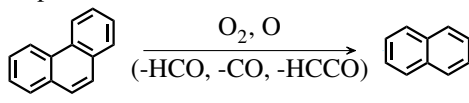
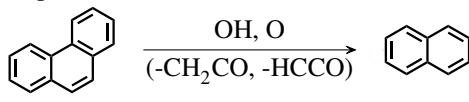
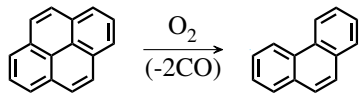
^aThe units are mole, centimetre, second, and kilocalorie.

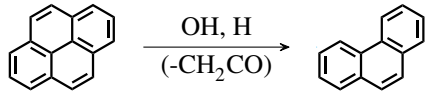
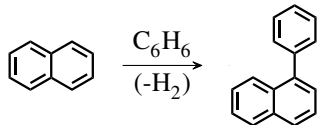
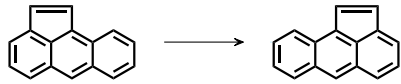
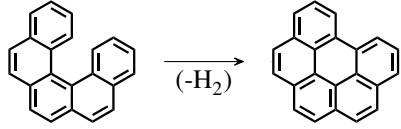
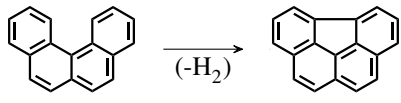
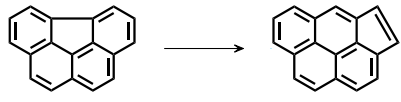
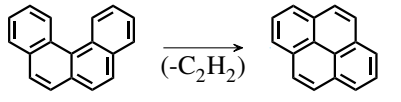
^bReactions with the sign “ \rightleftharpoons ” are reversible and those with “ \rightarrow ” are irreversible.

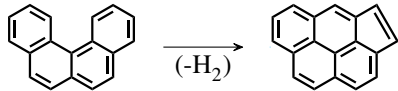
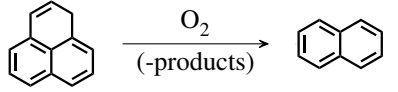
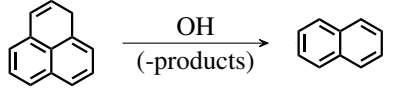
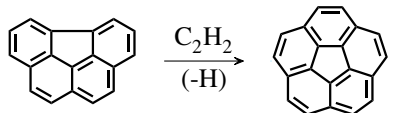
^cThe reverse rate coefficients were calculated via equilibrium constants.

Table S2: Kinetic Monte Carlo jump processes

Process [Ref.]	Parent site
S1 Free-edge ring growth [11]	Free-edge (FE)
Jump Process: 	Rate: $k_{12} \left(\frac{k_1[H] + k_8[OH]}{k_{-1a}[H_2] + k_6[H] + k_{-8}[H_2O] + k_{12}[C_2H_2]} \right) [C_2H_2][C_{FE}]$
S2 Armchair ring growth [11]	Armchair (AC)
Jump Process: 	Rate: $2k_{13} \left(\frac{k_1[H] + k_8[OH]}{k_{-1a}[H_2] + k_6[H] + k_{-8}[H_2O] + k_{13}[C_2H_2]} \right) [C_2H_2][C_{AC}]$
S3 Free-edge ring desorption [11]	Free-edge with two adjacent free-edges (FE3)
Jump Process: 	Rate: $k_{14} \left(\frac{k_1[H] + k_8[OH]}{k_{-1a}[H_2] + k_6[H] + k_{-8}[H_2O] + k_{14}} \right) [C_{FE3}]$
S4 6- to 5-member ring conversion at armchair [11]	Armchair next to FE3 (AC_{FE3})
Jump Process: 	Rate: $k_{15} \left(\frac{k_1[H] + k_8[OH]}{k_{-1a}[H_2] + k_6[H] + k_{-8}[H_2O] + k_{15}} \right) [C_{AC_{FE3}}]$

Process [Ref.]	Parent site
S5 5-member ring addition [11] Jump Process:  Rate: $k_{16} \left(\frac{k_1[\text{H}] + k_8[\text{OH}]}{k_{-1a}[\text{H}_2] + k_6[\text{H}] + k_{-8}[\text{H}_2\text{O}] + k_{16}[\text{C}_2\text{H}_2]} \right) [\text{C}_2\text{H}_2][\text{C}_{\text{ZZ}}]$	Zig-zag (ZZ)
S6 5-member ring desorption [11] Jump Process:  Rate: $k_{17} \left(\frac{k_9[\text{H}] + k_8[\text{OH}]}{k_{-9}[\text{H}_2] + k_{10}[\text{H}] + k_{-8}[\text{H}_2\text{O}] + k_{17}} \right) [\text{C}_{\text{R5}}]$	5-member ring (R5)
S7 5- to 6-member ring conversion at free edge [11] Jump Process:  Rate: $k_{12} \left(\frac{k_{11}[\text{H}]}{k_{-11} + k_{12}f[\text{C}_2\text{H}_2]} \right) f[\text{C}_2\text{H}_2][\text{C}_{\text{RFE}}],$ where $f = \left(\frac{k_1[\text{H}] + k_8[\text{OH}]}{k_{-1a}[\text{H}_2] + k_6[\text{H}] + k_{-8}[\text{H}_2\text{O}] + k_{12}[\text{C}_2\text{H}_2]} \right)$	5-member ring next to free-edge (RFE)
S8 5- to 6-member ring conversion at armchair [11] Jump Process:  Rate: $k_{18} \left(\frac{k_{11}[\text{H}] + k_8[\text{OH}]}{k_{-11} + k_{-8}[\text{H}_2\text{O}] + k_{18}} \right) [\text{C}_{\text{RAC}}]$	5-member ring next to armchair (RAC)
S9 Free-edge oxidation by O₂ [11] Jump Process:  Rate: $k_{19} \left(\frac{k_1[\text{H}] + k_8[\text{OH}]}{k_{-1a}[\text{H}_2] + k_6[\text{H}] + k_{-8}[\text{H}_2\text{O}] + k_{19}[\text{O}_2]} \right) [\text{O}_2][\text{C}_{\text{FE3}}]$	Free-edge with two adjacent free-edges (FE3)
S10 Free-edge oxidation by OH [11] Jump Process:  Rate: $k_{20}[\text{OH}][\text{C}_{\text{FE3}}]$	Free-edge with two adjacent free-edges (FE3)
S11 Armchair oxidation by O₂ [11] Jump Process:  Rate: $k_{21} \left(\frac{k_1[\text{H}] + k_8[\text{OH}]}{k_{-1a}[\text{H}_2] + k_6[\text{H}] + k_{-8}[\text{H}_2\text{O}] + k_{21}[\text{O}_2]} \right) [\text{O}_2][\text{C}_{\text{FE}_{\text{HACA}}}]$	Free-edge with two adjacent non-free-edges (FE_{HACA})

Process [Ref.]	Parent site
S12 Armchair oxidation by OH [11] Jump Process:  Rate: $k_{22}[\text{OH}][\text{C}_{\text{FEHACA}}]$	Free-edge with two adjacent non-free-edges (FE_{HACA})
S13 Benzene addition [33] Jump Process:  Rate: $k_{23} \left(\frac{k_1[\text{H}] + k_8[\text{OH}]}{k_{-1a}[\text{H}_2] + k_6[\text{H}] + k_{-8}[\text{H}_2\text{O}] + k_{23}[\text{C}_6\text{H}_6]} \right) [\text{C}_6\text{H}_6][\text{C}_s]$	All site types
S14 5-member ring migration [33] Jump Process:  Rate: $k_{24} \left(\frac{k_{11}[\text{H}] + k_8[\text{OH}]}{k_{-11} + k_{-8}[\text{H}_2\text{O}] + k_{24}} \right) [\text{C}_{\text{RZZ}}]$	5-member ring next to zig-zag (RZZ)
S15 6-member bay closure [33] Jump Process:  Rate: $2k_{25} \left(\frac{k_2[\text{H}] + k_8[\text{OH}]}{k_{-2}[\text{H}_2] + k_6[\text{H}] + k_{-8}[\text{H}_2\text{O}] + k_{25}} \right) [\text{C}_{\text{BY6}}]$	6-member bay (BY6)
S16 5-member bay closure [33] Jump Process:  Rate: $2k_{26} \left(\frac{k_3[\text{H}] + k_8[\text{OH}]}{k_{-1a}[\text{H}_2] + k_6[\text{H}] + k_{-8}[\text{H}_2\text{O}] + k_{26}} \right) [\text{C}_{\text{BY5}}]$	5-member bay (BY5)
S17 Embedded 5-member ring migration [33] Jump Process:  Rate: $k_{27} \left(\frac{k_4[\text{H}] + k_8[\text{OH}]}{k_{-1a}[\text{H}_2] + k_6[\text{H}] + k_{-8}[\text{H}_2\text{O}] + k_{27}} \right) [\text{C}_{\text{eR5}}]$	Embedded 5-member ring (eR5)
S18 6-member ring desorption at bay [34] Jump Process:  Rate: $k_{28} \left(\frac{k_5[\text{H}] + k_8[\text{OH}]}{k_{-1a}[\text{H}_2] + k_6[\text{H}] + k_{-8}[\text{H}_2\text{O}] + k_{28}} \right) [\text{C}_{\text{BY5FE3}}]$	BY5 next to FE3 (BY5_{FE3})

Process [Ref.]	Parent site
S19 6-member ring rearrangement at bay [34] Jump Process:  Rate: $\left[k_{28} \left(\frac{k_5[\text{H}] + k_8[\text{OH}]}{k_{-1a}[\text{H}_2] + k_6[\text{H}] + k_{-8}[\text{H}_2\text{O}] + k_{28}} \right) + k_7 \left(\frac{k_3[\text{H}] + k_8[\text{OH}]}{k_{-1a}[\text{H}_2] + k_6[\text{H}] + k_{-8}[\text{H}_2\text{O}] + k_7} \right) \right] [\text{C}_{\text{BY5FE3}}]$	BY5 next to FE3 (BY5_{FE3})
S20 Zig-zag oxidation by O₂ [60] Jump Process:  Rate: $k_{29} \left(\frac{k_1[\text{H}] + k_8[\text{OH}]}{k_{-1a}[\text{H}_2] + k_6[\text{H}] + k_{-8}[\text{H}_2\text{O}] + k_{29}[\text{O}_2]} \right) [\text{O}_2][\text{C}_{\text{FE2}}]$	Two adjacent free-edges (FE2)
S21 Zig-zag oxidation by OH [60] Jump Process:  Rate: $k_{30}[\text{OH}][\text{C}_{\text{FE2}}]$	Two adjacent free-edges (FE2)
S22 Capping of embedded 5-member ring Jump Process:  Rate: $k_{31} \left(\frac{k_1[\text{H}]}{k_{-1b}[\text{H}_2] + k_6[\text{H}] + k_{31}[\text{C}_2\text{H}_2]} \right) [\text{C}_2\text{H}_2][\text{C}_{\text{eR5}}]$	Embedded 5-member ring (eR5)

References

- [1] E. M. Adkins and J. H. Miller. Extinction measurements for optical band gap determination of soot in a series of nitrogen-diluted ethylene/air non-premixed flames. *Phys. Chem. Chem. Phys.*, 17:2686–2695, 2015. doi:10.1039/C4CP04452E.
- [2] N. L. Allinger, Y. H. Yuh, and J.-H. Lii. Molecular mechanics. The MM3 force field for hydrocarbons. 1. *J. Am. Chem. Soc.*, 111:8551–8566, 1989. doi:10.1021/ja00205a001.
- [3] B. Apicella, P. Pré, M. Alfè, A. Ciajolo, V. Gargiulo, C. Russo, A. Tregrossi, D. Deldique, and J. N. Rouzaud. Soot nanostructure evolution in premixed flames by

- high resolution electron transmission microscopy (HRTEM). *Proc. Combust. Inst.*, 35:1895–1902, 2015. doi:10.1016/j.proci.2014.06.121.
- [4] J. Appel, H. Bockhorn, and M. Frenklach. Kinetic modeling of soot formation with detailed chemistry and physics: laminar premixed flames of C₂ hydrocarbons. *Combust. Flame*, 121:122–136, 2000. doi:10.1016/S0010-2180(99)00135-2.
- [5] M. Balthasar and M. Kraft. A stochastic approach to calculate the particle size distribution function of soot particles in laminar premixed flames. *Combust. Flame*, 133:289–298, 2003. doi:10.1016/S0010-2180(03)00003-8.
- [6] F. Battin-Leclerc. Detailed chemical kinetic models for the low-temperature combustion of hydrocarbons with application to gasoline and diesel fuel surrogates. *Prog. Energy Combust. Sci.*, 34:440–498, 2008. doi:10.1016/j.pecs.2007.10.002.
- [7] O. Bonnet. Mémoire sur la théorie générale des surfaces. *J. de l'École Polytechnique*, 19:1–146, 1848.
- [8] M. L. Botero, E. M. Adkins, S. González-Calera, H. Miller, and M. Kraft. PAH structure analysis of soot in a non-premixed flame using high-resolution transmission electron microscopy and optical band gap analysis. *Combust. Flame*, 164:250–258, 2016. doi:10.1016/j.combustflame.2015.11.022.
- [9] M. L. Botero, D. Chen, S. González-Calera, D. Jefferson, and M. Kraft. HRTEM evaluation of soot particles produced by the non-premixed combustion of liquid fuels. *Carbon*, 96:459–473, 2016. doi:10.1016/j.carbon.2015.09.077.
- [10] F. W. Breyfogle III. *Implementing six sigma: smarter solutions using statistical methods*. John Wiley & Sons, New Jersey, 2003.
- [11] M. Celnik, A. Raj, R. West, R. Patterson, and M. Kraft. Aromatic site description of soot particles. *Combust. Flame*, 155:161–180, 2008. doi:10.1016/j.combustflame.2008.04.011.
- [12] D. Chen, Z. Zainuddin, E. Yapp, J. Akroyd, S. Mosbach, and M. Kraft. A fully coupled simulation of PAH and soot growth with a population balance model. *Proc. Combust. Inst.*, 34:1827–1835, 2013. doi:10.1016/j.proci.2012.06.089.
- [13] D. Chen, T. S. Totton, J. W. J. Akroyd, S. Mosbach, and M. Kraft. Size-dependent melting of polycyclic aromatic hydrocarbon nano-clusters: a molecular dynamics study. *Carbon*, 67:79–91, 2014. doi:10.1016/j.carbon.2013.09.058.
- [14] D. Chen, J. Akroyd, S. Mosbach, D. Opalka, and M. Kraft. Solid-liquid transitions in homogenous ovalene, hexabenzocoronene and circumcoronene clusters: a molecular dynamics study. *Combust. Flame*, 162:486–495, 2015. doi:10.1016/j.combustflame.2014.07.025.
- [15] A. Ciajolo, A. D'Anna, R. Barbella, A. Tregrossi, and A. Violi. The effect of temperature on soot inception in premixed ethylene flames. *Symp. (Int.) Combust.*, 26:2327–2333, 1996. doi:10.1016/S0082-0784(96)80061-0.

- [16] K. Crane, F. de Goes, M. Desbrun, and P. Schröder. Digital geometry processing with discrete exterior calculus. In C. Keenan (Ed.), *ACM SIGGRAPH 2013 courses* (pp. (16–18)). ACM: New York, 2013.
- [17] R. A. Dobbins, R. A. Fletcher, and H.-C. Chang. The evolution of soot precursor particles in a diffusion flame. *Combust. Flame*, 115:285–298, 1998. doi:10.1016/S0010-2180(98)00010-8.
- [18] M. Frenklach. On surface growth mechanism of soot particles. *Proc. Combust. Inst.*, 26:2285–2293, 1996. doi:10.1016/S0082-0784(96)80056-7.
- [19] M. Frenklach and L. B. Ebert. Comment on the proposed role of spheroidal carbon clusters in soot formation. *J. Phys. Chem.*, 92:561–563, 1988. doi:10.1021/j100313a061.
- [20] M. Frenklach and H. Wang. Detailed modeling of soot particle nucleation and growth. *Proc. Combust. Inst.*, 23:1559–1566, 1990. doi:10.1016/S0082-0784(06)80426-1.
- [21] M. Frenklach and H. Wang. Detailed mechanism and modeling of soot particle formation. In H. Bockhorn (Ed.), *Soot Formation in Combustion—Mechanisms and Models* (pp. (165–190)). Springer: Berlin, 1994.
- [22] M. Frenklach, N. W. Moriarty, and N. J. Brown. Hydrogen migration in polyaromatic growth. *Symp. (Int.) Combust.*, 27:1655–1661, 1998. doi:10.1016/S0082-0784(98)80004-0.
- [23] M. Frenklach, C. A. Schuetz, and J. Ping. Migration mechanism of aromatic-edge growth. *Proc. Combust. Inst.*, 30:1389–1396, 2005. doi:10.1016/j.proci.2004.07.048.
- [24] C. F. Gauss. Disquisitiones generales circas superficies curvas. *Comment. Soc. Reg. Sci. Göttingen. Rec.*, 6, 1828.
- [25] Ph. Gerhardt, S. Löffler, and K. H. Homann. Polyhedral carbon ions in hydrocarbon flames. *Chem. Phys. Lett.*, 137:306–310, 1987. doi:10.1016/0009-2614(87)80889-8.
- [26] W. J. Grieco, J. B. Howard, L. C. Rainey, and J. B. Vander Sande. Fullerenic carbon in combustion-generated soot. *Carbon*, 38:597–614, 2000. doi:10.1016/S0008-6223(99)00149-9.
- [27] K.-H. Homann. Fullerenes and soot formation—new pathways to large particles in flames. *Angew. Chem. Int. Ed.*, 37:2434–2451, 1998. doi:10.1002/(SICI)1521-3773(19981002)37:18<2434::AID-ANIE2434>3.0.CO;2-L.
- [28] R. J. Kee, J. F. Grcar, M. D. Smooke, and J. A. Miller. PREMIX: a FORTRAN program for modeling steady laminar one-dimensional premixed flames. Report No. SAND85-8240, Sandia National Laboratories, Livermore, CA, USA, 1985.
- [29] H. W. Kroto, J. R. Heath, S. C. O’Brien, R. F. Curl, and R. E. Smalley. C60: buckminsterfullerene. *Nature*, 318:162–163, 1985. doi:10.1038/318162a0.

- [30] S. Lijima, T. Ichihashi, and Y. Ando. Pentagons, heptagons and negative curvature in graphite microtubule growth. *Nature*, 356:776–778, 1992. doi:10.1038/356776a0.
- [31] S. Mosbach, M. S. Celnik, A. Raj, M. Kraft, H. R. Zhang, S. Kubo, and K.-O. Kim. Towards a detailed soot model for internal combustion engines. *Combust. Flame*, 156:1156–1165, 2009. doi:10.1016/j.combustflame.2009.01.003.
- [32] R. L. Murry, J. R. Colt, and G. E. Scuseria. How accurate are molecular mechanics predictions for fullerenes? A benchmark comparison with Hartree-Fock self-consistent field results. *J. Phys. Chem.*, 97:4954–4959, 1993. doi:10.1021/j100121a016.
- [33] A. Raj, M. Celnik, R. Shirley, M. Sander, R. Patterson, R. West, and M. Kraft. A statistical approach to develop a detailed soot growth model using PAH characteristics. *Combust. Flame*, 156:896–913, 2009. doi:10.1016/j.combustflame.2009.01.005.
- [34] A. Raj, P. L. W. Man, T. S. Totton, M. Sander, R. A. Shirley, and M. Kraft. New polycyclic aromatic hydrocarbon (PAH) surface processes to improve the model prediction of the composition of combustion-generated PAHs and soot. *Carbon*, 48:319–332, 2010. doi:10.1016/j.carbon.2009.09.030.
- [35] K. L. Revzan, N. J. Brown, and M. Frenklach. <http://www.me.berkeley.edu/soot>.
- [36] H. Richter, S. Granata, W. H. Green, and J. B. Howard. Detailed modeling of PAH and soot formation in a laminar premixed benzene/oxygen/argon low-pressure flame. *Proc. Combust. Inst.*, 30:1397–1405, 2005. doi:10.1016/j.proci.2004.08.088.
- [37] J. Robertson and E. P. O’Reilly. Electronic and atomic structure of amorphous carbon. *Phys. Rev. B*, 35:2946–2957, 1987. doi:10.1103/PhysRevB.35.2946.
- [38] C. Russo, F. Stanzione, A. Tregrossi, M. Alfè, and A. Ciajolo. The effect of temperature on the condensed phases formed in fuel-rich premixed benzene flames. *Combust. Flame*, 159:2233–2242, 2012. doi:10.1016/j.combustflame.2012.02.014.
- [39] H. Sabbah, L. Biennier, S. J. Klippenstein, I. R. Sims, and B. R. Rowe. Exploring the role of PAHs in the formation of soot: pyrene dimerization. *J. Phys. Chem. Lett.*, 1:2962–2967, 2010. doi:10.1021/jz101033t.
- [40] M. Sander, R. I. A. Patterson, A. Braumann, A. Raj, and M. Kraft. Developing the PAH-PP soot particle model using process informatics and uncertainty propagation. *Proc. Combust. Inst.*, 33:675–683, 2011. doi:10.1016/j.proci.2010.06.156.
- [41] C. A. Schuetz and M. Frenklach. Nucleation of soot: molecular dynamics simulations of pyrene dimerization. *Proc. Combust. Inst.*, 29:2307–2314, 2002. doi:10.1016/S1540-7489(02)80281-4.
- [42] R. I. Singh, A. M. Mebel, and M. Frenklach. Oxidation of graphene-edge six- and five-member rings by molecular oxygen. *J. Phys. Chem. A*, 119:7528–7547, 2015. doi:10.1021/acs.jpca.5b00868.

- [43] J. J. P. Stewart. Quantum Chemistry Exchange Program No. 455, Indiana University, Bloomington, IN, 1983; CS Chem3D 15.1, CambridgeSoft, Cambridge, MA, 2016.
- [44] P. D. Teini, D. M. A. Karwat, and A. Atreya. Observations of nascent soot: molecular deposition and particle morphology. *Combust. Flame*, 158:2045–2055, 2011. doi:10.1016/j.combustflame.2011.03.005.
- [45] T. S. Totton, D. Chakrabarti, A. J. Misquitta, M. Sander, D. J. Wales, and M. Kraft. Modelling the internal structure of nascent soot particles. *Combust. Flame*, 157:909–914, 2010. doi:10.1016/j.combustflame.2009.11.013.
- [46] T. S. Totton, A. J. Misquitta, and M. Kraft. A quantitative study of the clustering of polycyclic aromatic hydrocarbons at high temperatures. *Phys. Chem. Chem. Phys.*, 14:4081–4094, 2012. doi:10.1039/c2cp23008a.
- [47] R. L. Vander Wal and A. J. Tomasek. Soot oxidation: dependence upon initial nanostructure. *Combust. Flame*, 134:1–9, 2003. doi:10.1016/S0010-2180(03)00084-1.
- [48] A. Violi. Modeling of soot particle inception in aromatic and aliphatic premixed flames. *Combust. Flame*, 139:279–287, 2004. doi:10.1016/j.combustflame.2004.08.013.
- [49] A. Violi. Cyclodehydrogenation reactions to cyclopentafused polycyclic aromatic hydrocarbons. *J. Phys. Chem. A*, 109:7781–7787, 2005. doi:10.1021/jp052384r.
- [50] A. Violi, A. Kubota, T. N. Truong, W. J. Pitz, C. K. Westbrook, and A. F. Sarofim. A fully integrated kinetic Monte Carlo/molecular dynamics approach for the simulation of soot precursor growth. *Proc. Combust. Inst.*, 29:2343–2349, 2002. doi:10.1016/S1540-7489(02)80285-1.
- [51] A. Violi, A. F. Sarofim, and G. A. Voth. Kinetic Monte Carlo–molecular dynamics approach to model soot inception. *Combust. Sci. Technol.*, 176:991–1005, 2004. doi:10.1080/00102200490428594.
- [52] H. Wang. Formation of nascent soot and other condensed-phase materials in flames. *Proc. Combust. Inst.*, 33:41–67, 2011. doi:10.1016/j.proci.2010.09.009.
- [53] H. Wang and M. Frenklach. A detailed kinetic modeling study of aromatics formation in laminar premixed acetylene and ethylene flames. *Combust. Flame*, 110:173–221, 1997. doi:10.1016/S0010-2180(97)00068-0.
- [54] H. Wang, D. X. Du, C. J. Sung, and C. K. Law. Experiments and numerical simulation on soot formation in opposed-jet ethylene diffusion flames. *Symp. (Int.) Combust.*, 26:2359–2368, 1996. doi:10.1016/S0082-0784(96)80065-8.
- [55] H. Wang, B. Zhao, B. Wyslouzil, and K. Streletzky. Small-angle neutron scattering of soot formed in laminar premixed ethylene flames. *Proc. Combust. Inst.*, 29:2749–2757, 2002. doi:10.1016/S1540-7489(02)80335-2.

- [56] R. Whitesides and M. Frenklach. Detailed kinetic Monte Carlo simulations of graphene-edge growth. *J. Phys. Chem. A*, 114:689–703, 2010. doi:10.1021/jp906541a.
- [57] R. Whitesides and M. Frenklach. Effect of reaction kinetics on graphene-edge morphology and composition. *Z. Phys. Chem.*, 229:597–614, 2014. doi:10.1515/zpch-2014-0633.
- [58] R. Whitesides, D. Domin, R. Salomón-Ferrer, W. A. Lester Jr., and M. Frenklach. Embedded-ring migration on graphene zigzag edge. *Proc. Combust. Inst.*, 32:577–583, 2009. doi:10.1016/j.proci.2008.06.096.
- [59] E. K. Y. Yapp, D. Chen, J. Akroyd, S. Mosbach, M. Kraft, J. Camacho, and H. Wang. Numerical simulation and parametric sensitivity study of particle size distributions in a burner-stabilised stagnation flame. *Combust. Flame*, 162:2569–2581, 2015. doi:10.1016/j.combustflame.2015.03.006.
- [60] E. K. Y. Yapp, R. I. A. Patterson, J. Akroyd, S. Mosbach, E. M. Adkins, J. H. Miller, and M. Kraft. Numerical simulation and parametric sensitivity study of optical band gap in a laminar co-flow ethylene diffusion flame. *Combust. Flame*, 167:320–334, 2016. doi:10.1016/j.combustflame.2016.01.033.
- [61] X. You, R. Whitesides, D. Zubarev, W. A. Lester Jr., and M. Frenklach. Bay-capping reactions: kinetics and influence on graphene-edge growth. *Proc. Combust. Inst.*, 33: 685–692, 2011. doi:10.1016/j.proci.2010.05.110.